A. Rausa, A. Guardone, F. Auteri
Implementation of [Gamma]-Re0 Transition Model within SU2: Model Validation and Verification
in: AIAA Scitech 2023 Forum, AIAA, 2023, ISBN: 9781624106996, p. 1-23, AIAA 2023-1570
[AIAA Scitech 2023 Forum, National Harbor, MD, USA & Online, 23-27 Jan. 2023]
doi:10.2514/6.2023-1570

Implementation of γ-Re_θ transition model within SU2: model validation

Rausa A.*, Guardone A. †, Auteri F. ‡
Politecnico di Milano, Milano, Italy, 20154

In this work, the γ-Re_θ (LM) transition model has been implemented within the open-source CFD framework SU2. The model is based on two transport equations, one for intermittency and one for a transition onset criterion in terms of momentum-thickness Reynolds number. Transition-to-turbulence models coupling has been implemented for both the Spalart-Allmaras and the Menter SST models. The LM2015 variant has been implemented to assess the capability of predicting crossflow-induced transition on 3D test cases. Extensive validation has been performed on consolidated benchmarks on both 2D and 3D geometries. Numerical results are in good agreement on the whole range of test cases.

I. Introduction

Laminar-to-turbulent transition modeling is a hot topic among the CFD community due to the difficulty in correctly predicting this phenomenon. One of the reasons is that transition occurs through different mechanisms in different applications. For example, in aerodynamic flows, both *natural* and *separated induced* transition can occur. The first refers to flow instability, which eventually leads to a nonlinear breakdown of turbulence. The latter is encountered where a laminar boundary layer separates under a pressure gradient, and transition develops within the separated shear layer. Another transition phenomenon is called *bypass* transition, where the development of turbulence is abrupt due to the high values of free-stream turbulence intensity, which is typical for turbo-machinery-related flows.

Different methodologies have been developed to tackle this problem. Some of these are CFD-compatible, whereas others are not due to the need for non-local information or streamline integrations. For example, the e^n method of Smith and Gamberoni [1] and van Ingen [2] require a priori knowledge of geometry and grid topology. Plus, they require numerous non-local operations, thus making them incompatible with modern general-purpose CFD codes.

Another approach is to use the Low-Reynolds (Re) number turbulence models [3][4], where the wall damping functions of the underlying turbulence model trigger the transition onset. However, at best, these models can only be expected to simulate bypass transition. Indeed, regarding the other transition mechanisms, there is no proven reason they should be able to predict a flow phenomenon for which they are not calibrated.

The last approach is the use of empirical correlations which usually correlates the turbulence intensity at the free-stream (FSTI) with the momentum-thickness Reynolds number ($Re_{\theta t}$) at transition onset [5]. Although this approach has a broad experimental agreement, it is challenging to implement in CFD codes since it requires knowledge of the boundary layer thickness θ. This is not readily available in general Navier-Stokes software, especially if unstructured grids are considered. The solution to this problem has been proposed by Menter at al. [6][7][8] through the implementation of two PDEs, one for the intermittency and one for the momentum thickness Reynolds number. The first one is used to switch between laminar and turbulent flow by activating the production term for the turbulence model. The latter removes the non-local information required by the empirical correlations. Other intermittency-based models have been developed, which are algebraic, thus, do not require any new PDE. Among these are Mura and Bas [9] and Kubacki et al. [10]. Both obtain good results, demonstrating that an equivalent level of predictive capability compared with the higher-order models can be obtained as long as correctly modeled physics is maintained.

In this paper, the Langtry-Menter transition model has been implemented within the SU2 suite to enrich its prediction capabilities. Transition-to-turbulence coupling has been performed for both the Spalart-Allmaras and the Menter SST turbulence models. The LM2015 variant has been added to predict crossflow induced transition for 3D test cases. The validity of the implementation has been verified against well-known transition test cases, including both 2D and 3D simulations.

*PhD Student, Department of Aerospace Science and Technology, andrea.rausa@polimi.it
†Full Professor, Department of Aerospace Science and Technology, alberto.guardone@polimi.it
‡Associate Professor, Department of Aerospace Science and Technology, franco.auteri@polimi.it

This abstract is organized as follows. Section II will report the numerical treatment of the transition model and its coupling with the turbulence model. Section III will present the validation test cases. Here, the numerical results will be compared against experimental data to highlight the prediction capabilities of the LM model. Finally, Sec. IV will provide conclusions to this work.

II. Numerical setup

SU2 [11] is an open-source suite used for solving Partial Differential Equations (PDEs) on unstructured grids. The Finite Volume Method (FVM) is applied using a standard edge-based data structure on a dual grid with control volumes constructed using a median-dual, vertex-based scheme. Median-dual control volumes are formed by connecting centroids, face, and edge midpoints of all primal cells sharing the particular vertex. After integration of the Navier-Stokes equations over a control volume Ω_i, the following residual-based formulation can be obtained:

$$\begin{aligned} 0 &= \int_{\Omega_i} \frac{\partial U}{\partial t} d\Omega + \sum_{j \in \mathbb{N}(i)} (\tilde{F}^c_{ij} + \tilde{F}^v_{ij}) \Delta S_{ij} - Q|\Omega_i| \\ &= \int_{\Omega_i} \frac{\partial U}{\partial t} d\Omega + R_i(U), \end{aligned} \tag{1}$$

where $R_i(U)$ is the numerical residual that represents the integration of all spatial terms for the control volume surrounding vertex i. $\tilde{F}^c_{ij}$ and $\tilde{F}^v_{ij}$ are the numerical approximations of the convective and viscous fluxes projected along an edge, respectively, and Q is the source term. ΔS_{ij} is the area of the face associated with the edge ij and $\mathbb{N}(i)$ is the set of neighboring vertices to vertex i. In this work, both compressible and incompressible simulations will be performed. In the former case, we make use of the upwind Roe scheme for the discretization of the convective fluxes of the mean flow. In the latter, we adopt the Flux-Difference Splitting scheme (FDS). In both cases, a MUSCL approach is employed for achieving a second-order reconstruction. The Venkatakrishnan flux limiter has been applied to avoid local solution oscillation by limiting the gradients during high-order reconstruction.

A. Turbulence modeling

Following the Boussinesq hypothesis, the effect of turbulence is represented as an increased viscosity, thus leading to the computation of the total viscosity as the sum of a laminar viscosity μ and of a turbulent viscosity μ_t. The latter is modeled through either the industry-standard Menter Shear Stress Transport (SST) [12] turbulence model or the Spalart-Allmaras turbulence model. The first one introduces two transport equations: one for the turbulent kinetic energy (k) and one for the turbulent frequency (ω). These equations can be written in differential form as:

$$\begin{aligned} &\frac{\partial(\rho\, k)}{\partial t} + \frac{\partial(\rho\, u_j\, k)}{\partial x_j} = \tilde{P}_k - \tilde{D}_k + \frac{\partial}{\partial x_j}\left[(\mu + \sigma_k\, \mu_t)\frac{\partial k}{\partial x_j}\right] \\ &\frac{\partial(\rho\, \omega)}{\partial t} + \frac{\partial(\rho\, u_j\, \omega)}{\partial x_j} = \alpha \frac{\tilde{P}_k}{\nu_t} - D_\omega + CD_{k\omega} + \frac{\partial}{\partial x_j}\left[(\mu + \sigma_k\, \mu_t)\frac{\partial \omega}{\partial x_j}\right] \end{aligned} \tag{2}$$

where $\tilde{P}_k$ and $\tilde{D}_k$ are respectively the modified production and modified destruction terms for the variable k, σ_k and α are model constants, D_ω is the destruction term for the variable ω and $CD_{k\omega}$ is the cross-diffusion term. The new variables k and ω are directly related to the turbulence viscosity through the following formulation:

$$\begin{aligned} &\mu_t = \frac{\rho a_1 k}{\max(a_1\omega, \Omega F_2)}, \quad \Omega = \sqrt{W_{ij}W_{ij}}, \quad W_{ij} = \frac{1}{2}\left(\frac{\partial u_i}{\partial x_j} - \frac{\partial u_j}{\partial x_i}\right) \\ &F_2 = \tanh\left(\mathrm{arg}_2^2\right), \quad arg_2 = \max\left(2\frac{\sqrt{k}}{\beta^* \omega d}, \frac{500\nu}{d^2\omega}\right) \end{aligned} \tag{3}$$

where $a_1 = 0.31$ is a constant of the model, Ω is the vorticity magnitude and F_2 is a model function.

In the case of the Spalart-Allmaras (SA) turbulence model [13], the turbulent viscosity is computed as:

$$\mu_t = \rho \hat{\nu} f_{v1}, \quad f_{v1} = \frac{\chi^3}{\chi^3 + c_{v1}^3}, \quad \chi = \frac{\hat{\nu}}{\nu}, \quad \nu = \frac{\mu_d}{\rho} \tag{4}$$

and the new variable $\hat{\nu}$ is obtained solving the following transport equation

$$\frac{\partial(\rho\, \hat{\nu})}{\partial t} + \frac{\partial(\rho\, u_j\, \hat{\nu})}{\partial x_j} = \tilde{P}_{\hat{\nu}} - \tilde{D}_{\hat{\nu}} + \frac{\partial}{\partial x_j}\left[\left(\frac{\hat{\nu} + \nu}{\sigma}\right)\frac{\partial \hat{\nu}}{\partial x_j}\right] \tag{5}$$

where $\tilde{P}_{\hat{\nu}}$ and $\tilde{D}_{\hat{\nu}}$ are respectively the modified production and modified destruction terms for the variable $\hat{\nu}$, and $\sigma = 2/3$ is a constant of the model.

B. Transition modeling

Laminar-to-turbulent transition is computed through the γ-Re_θ model (Langtry-Menter, LM) [14], which introduces two new sets of PDEs for the intermittency (γ) and the momentum-thickness Reynolds number ($\tilde{Re}_{\theta t}$), defined as:

$$\begin{aligned} \frac{\partial(\rho\,\gamma)}{\partial t} + \frac{\partial(\rho\,u_j\,\gamma)}{\partial x_j} &= \tilde{P}_\gamma - \tilde{D}_\gamma + \frac{\partial}{\partial x_j}\left[(\mu + \frac{\mu_t}{\sigma_f})\frac{\partial \gamma}{\partial x_j}\right] \\ \frac{\partial(\rho\,\tilde{Re}_{\theta t})}{\partial t} + \frac{\partial(\rho\,u_j\,\tilde{Re}_{\theta t})}{\partial x_j} &= \tilde{P}_{\theta t} + \frac{\partial}{\partial x_j}\left[\sigma_{\theta t}(\mu + \mu_t)\frac{\partial \tilde{Re}_{\theta t}}{\partial x_j}\right] \end{aligned} \tag{6}$$

where $\tilde{P}_\gamma$ and $\tilde{D}_\gamma$ are respectively the production and destruction terms for the variable γ, $\sigma_f = 1.0$ and $\sigma_{\theta t} = 2.0$ are model constants and $\tilde{P}_{\theta t}$ is the production term for the variable $\tilde{Re}_{\theta t}$.

Different enhancements can be applied to the model in order to include various effects that will influence transition onset, such as the so-called cross-flow extension [15] and the compressibility correction [16]. The first one has been implemented in the form of the LM2015 model, following the paper by Menter et al. [17]. However, the in-depth description of this model (and of the turbulence one) is out of the scope of this paper and will thus be omitted.

The transition model is coupled to the turbulence one through the modification of the production and destruction terms of the turbulence equations. In the case of the Menter-SST model, following the original work by Menter et al. [14], the modifications are made on the production and destruction terms for the turbulent kinetic energy and on the blending function F_1 responsible for switching between the $k-\omega$ and $k-\epsilon$ models. In particular, one can define the new terms as:

$$\begin{aligned} &\tilde{P}_k = \gamma_{eff} P_k \quad \tilde{D}_k = \min(\max(\gamma_{eff}, 0.1)1.0) D_k \\ &R_y = \frac{\rho y \sqrt{k}}{\mu}; \quad F_3 = e^{-\left(\frac{R_y}{120}\right)^8}; \quad \tilde{F}_1 = \max(F_1, F_3). \end{aligned} \tag{7}$$

Where γ_{eff} is the effective intermittency and is computed as the maximum between γ and γ_{sep}, which is in turn defined as the intermittency used for predicting separation-induced transition.

Regarding the Spalart-Allmaras turbulence model, following the work of D'Alessandro et al. [18], the transition augmentation is implemented through modification of the production and destruction term for the variable $\hat{\nu}$:

$$\tilde{P}_{\hat{\nu}} = \gamma_{eff} P_{\hat{\nu}} \quad \tilde{D}_{\hat{\nu}} = \min(\max(\gamma, 0.5)1.0) D_{\hat{\nu}} \tag{8}$$

Although the original formulation for the new destruction term $\tilde{D\nu}$ is reported as:

$$\tilde{D}_{\hat{\nu}} = \max(\min(\gamma, 0.5)1.0) D_{\hat{\nu}} \tag{9}$$

it is believed to be a typing mistake since the multiplicative coefficient applied to $D_{\hat{\nu}}$ is always 1. Thus the destruction term is not influenced by the intermittency parameter and will always be equal to the fully-turbulent value, which is not desired.

Both the turbulent and transition convective fluxes are obtained through a first-order upwind scheme with MUSCL reconstruction.

In this work, steady-state simulations are mainly performed. The implicit Euler scheme has been used to advance the computation within a fictitious time step. The convergence of the solution is obtained when the minimum value of the base 10 logarithm of the root mean squared residual of ρ is below a user-defined threshold.

III. Results

A. 2D Test Cases

This section reports the validation results of the implemented transition model on 2D test cases. The benchmarks taken into consideration are the European Research Community on Flow Turbulence and Combustion (ERCOFTAC) T3 series of flat-plate experiments [19][20], the Schubauer and Klebanoff (S&K) flat-plate experiment [21] and the E387 experiments by McGhee et al. at Langley low-turbulence pressure tunnel (LTPT) [22].

1. Flat Plate test cases

The Zero-Pressure-Gradient (ZPG) test cases were performed on a 1.5-meter-long flat plate with a very smooth surface. The transition process associated with these experiments varies from moderately high- to low- turbulence intensity bypass transition, comprehending natural transition for the S&K case. Skin friction coefficient values are available from the literature and have been used to validate the numerical results.

The inlet conditions for each test case, namely the inlet velocity U, the free-stream turbulence intensity (FSTI), the turbulence-to-laminar viscosity ratio (μ_t/μ), the density (ρ), and the laminar viscosity (μ), are reported in Tab. 1.

Table 1 Inlet conditions for ZPG flat plate test-cases

Case	**U inlet** (m/s)	**FSTI inlet** (%)	$\boldsymbol{\mu_t/\mu}$	$\boldsymbol{\rho}$ (kg/m^3)	$\boldsymbol{\mu}$ (kg/ms)
T3A	5.4	3.5	13.3	1.2	1.8×10^{-5}
T3B	9.4	6.5	100.0	1.2	1.8×10^{-5}
T3A-	19.8	0.874	8.72	1.2	1.8×10^{-5}
S&K	50.1	0.18	5.0	1.2	1.8×10^{-5}

Following the guidelines in [23], the computational mesh extends for 0.15 m upstream of the leading edge of the flat plate and for 1.7 m downstream. The upper wall is at a distance of 0.3 m. Slip wall conditions have been imposed on the plate's top and lower boundary upstream. No-slip boundary conditions have been imposed on the plate. Inlet conditions are enforced on the left boundary through a specified velocity profile, while zero-pressure gradient outlet condition has been imposed on the right boundary. The spacing on the leading edge has been set to 0.001 m, while the spacing on the other extreme is set to 0.01 m. The *tanh* function has been used to discretize the points distribution on the plate. The vertical spacing follows an exponential growth function as a geometric progression. The growth rate is equal to 1.1, and the first cell height is set to 10^{-6} m while the last cell height of the progression is equal to 0.01 m. This ensures that the y^+ is well below 1 for all test cases. The horizontal spacing value at the inlet boundary equals 0.01 m. This setup results in a mesh of size 470×110 points, with 435 points on the plate. A mesh convergence study has been performed by halving (or doubling) the spacing constraints at the extremes of both the flat plate and the inlet boundary. The growth rate has ranged between 1.075 for the finest mesh and 1.2 for the coarsest one. The properties of the meshes used for this study are summarized in Tab. 2.

Table 2 Mesh properties for convergence study of ZPG flat plate test-cases

Refinement Level	**LE Spacing**	**End Plate and Inlet Spacings**	$\boldsymbol{\Delta s_0}$	**Growth rate**	**N° of elements**
T (Tiny)	0.008	0.08	8×10^{-6}	1.2	58×46
C (Coarse)	0.004	0.04	4×10^{-6}	1.15	118×62
M (Medium)	0.002	0.02	2×10^{-6}	1.125	236×79
F (Fine)	0.001	0.01	1×10^{-6}	1.1	470×110
X (Extra Fine)	0.0005	0.005	5×10^{-7}	1.075	946×175
U (Ultra Fine)	0.00025	0.0025	2.5×10^{-7}	1.05	1893×290

As reference results for the mesh convergence study, those on the S&K test case are reported in Fig. 1.

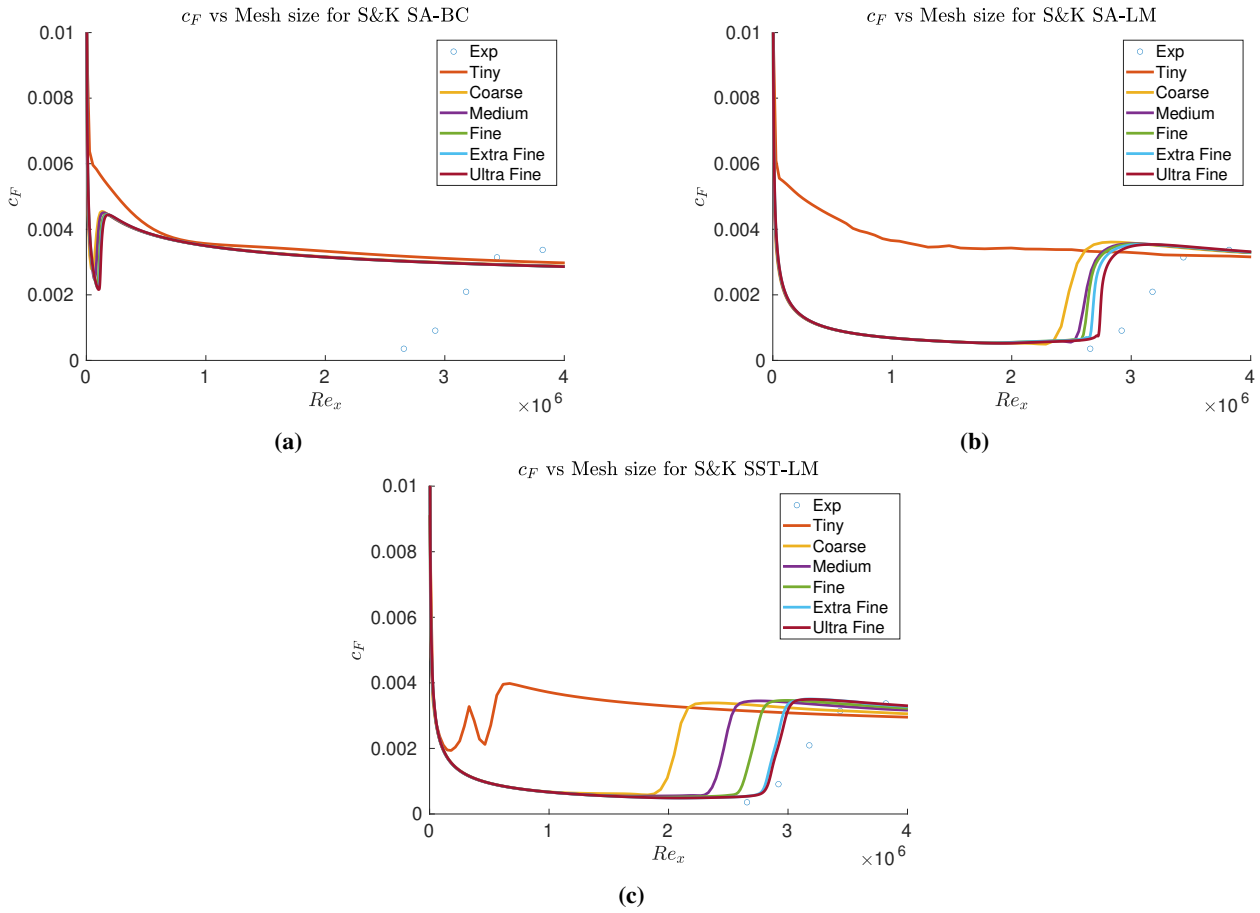

Fig. 1 Mesh convergence for S&K Flat Plate test case

Mesh convergence has been achieved with the extra fine mesh for all the transition-turbulence model's couplings. Once the computational mesh has been obtained, CFD computations have been performed. In Fig. 2 the skin friction coefficient (C_F) on the flat plate is compared against the experimental results. To evaluate the performance of the transition model, results obtained with the Bas-Cakmakcioglu [9] model (BC) coupled with the Spalart-Allmaras turbulence model are also reported.

The results obtained through the LM model agree with the experiments, whereas the BC model over-predicts the transition onset location. When coupled with the SST turbulence model, the former seems to struggle only on the S&K test case, probably due to the low value of free-stream turbulence intensity. When coupled with the SA model, the transition prediction is poor across all of the test cases except for the S&K case. In particular, SA-LM struggles when dealing with high freestream turbulence intensities, like those encountered in the T3A and T3B test cases. The model seems to predict the transition, but the skin friction coefficient never reaches the fully-turbulent value, indicating that the flow remains in an intermediate state. This is not physical and seems to be related to the SA turbulence model, as the SST-LM coupling does not exhibit this behavior.

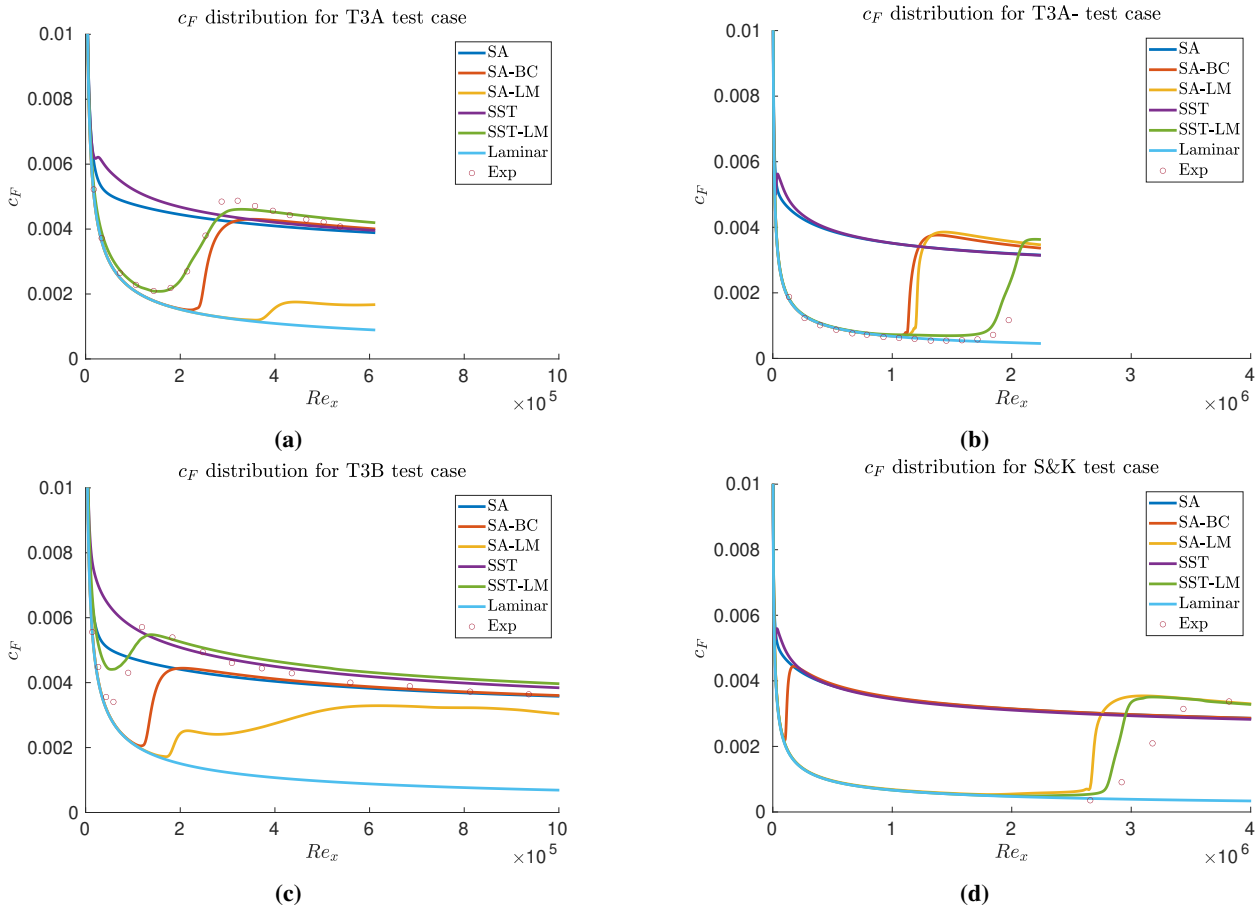

Fig. 2 Skin Friction Coefficient (C_F) for ZPG Flat Plate test-cases: comparison among Langtry-Menter transition model (LM), Bas-Cakmakcioglu transition model (BC), fully-turbulent (SST), laminar (NS)

2. E387 test case

The E387 profile is attractive due to the presence of laminar separation bubbles (LSBs) with turbulent reattachment, which fully-turbulent simulations cannot predict. The operative conditions are reported in Tab. 3.

Table 3 Operating conditions for E387 test-case

Test parameters	Value
Reynolds number (Re)	2×10^5
Mach number (Ma)	0.06
Free-stream temperature (T_∞)	288.15 K
Reynolds length (Re_L)	1 m
Angle of Attack (α)	$[0° \div 16°]$
Free-stream turbulence intensity (FSTI)	0.1 %

The computational mesh has an O-grid topology with 824×178 cells. The first cell height is equal to 10^{-5} m and ensures $y^+ < 1$. The grid is obtained through the hyperbolic extrusion of the profile following a geometric progression with a growth rate of 1.075. The far field extends for 50 chords away from the profile.

In Fig. 3 and Fig. 4 the pressure distribution over the E387 airfoil is compared for different angles of attack across the LM model, the BC model, and fully-turbulent SST and SA simulations. Two different numerical schemes have been used to compute the convective numerical fluxes: the ROE scheme and the L2ROE scheme. The latter has been

chosen since it introduces numerical corrections to account for the low Reynolds and Mach numbers involved in these simulations.

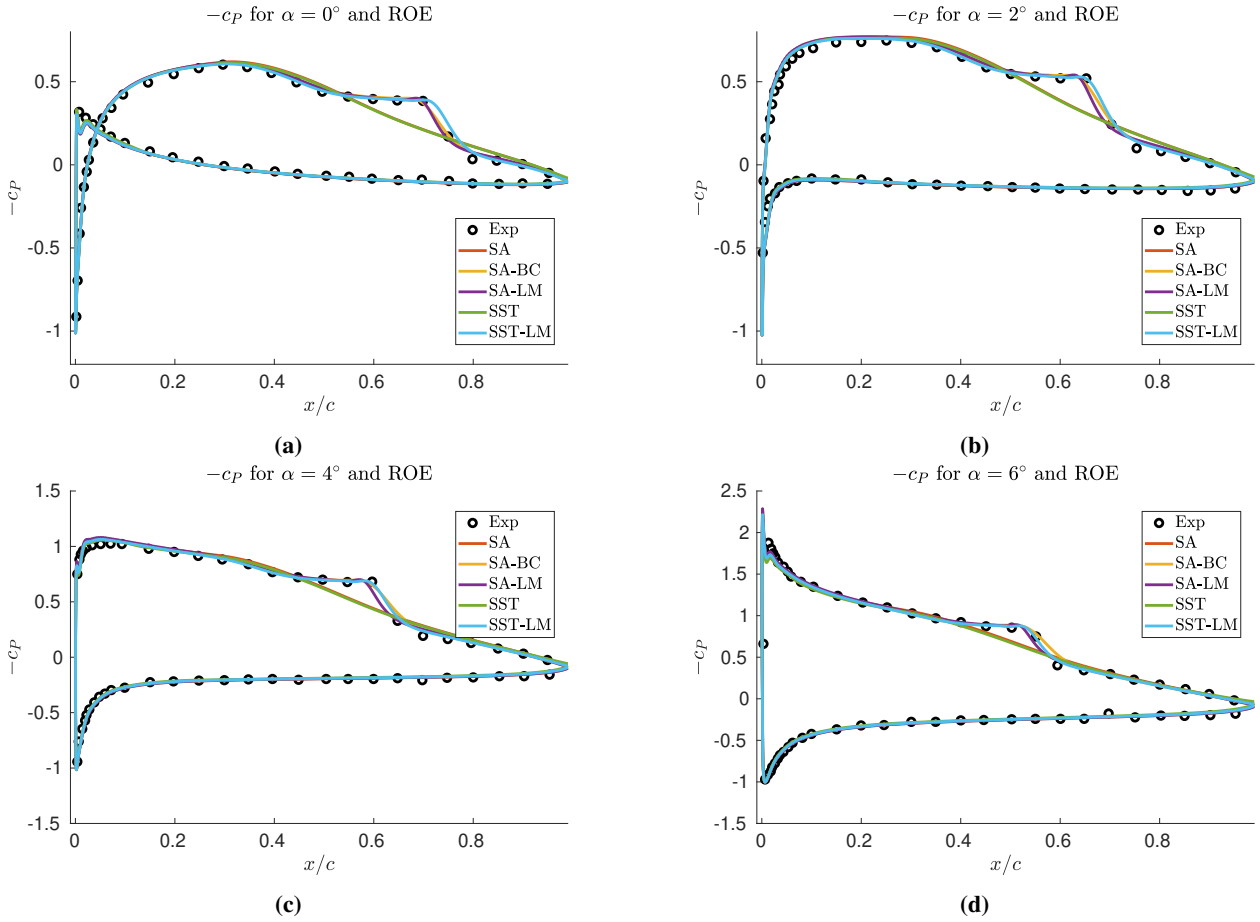

Fig. 3 Pressure coefficient distribution over E387 profile with ROE scheme

The advantage of coupling a transition model over the fully-turbulent simulation is clear: the laminar separation bubble and the turbulent reattachment are well-predicted by both the LM and the BC model, whereas they are not present in the fully-turbulent computation. The SST-LM couple consistently predicts LSBs slightly further downstream than the SA-LM model. However, the extension of these recirculating regions seems similar, pointing to the increase in k and in $\hat{\nu}$ due to boundary layer separation being of a similar entity. The SA-BC model, instead, predicts larger separation bubbles than the SA-LM model with both the ROE and the L2ROE scheme. It also computes a further reattachment point than SST-LM in the case of the L2ROE scheme. In all cases, the transition models allow for the prediction of LSBs, which translates into a better agreement between the numerical simulations and experimental results regarding the drag coefficient, as seen from the inspection of Fig. 5. The C_L-α curve is well-predicted by the LM model across the whole range of angles of attack, including the post-stall regime. The activation of the transition model also improves the prediction of the maximum C_L and the stall angle, especially when the couple SA-LM is considered. This can be seen for both the ROE and the L2ROE scheme. However, when the L2ROE scheme is considered, the BC model deviates marginally when compared with the SA-LM model at high angles of attack, as can be seen from Fig. 5c. In particular, the stall angle is under-predicted by 2 degrees, after which the lift coefficient seems to raise again instead of remaining almost constant, as suggested by the experimental results. It probably points to the existence of an unsteady solution. Thus, Unsteady-RANS (URANS) computations should be performed to assess this observation.

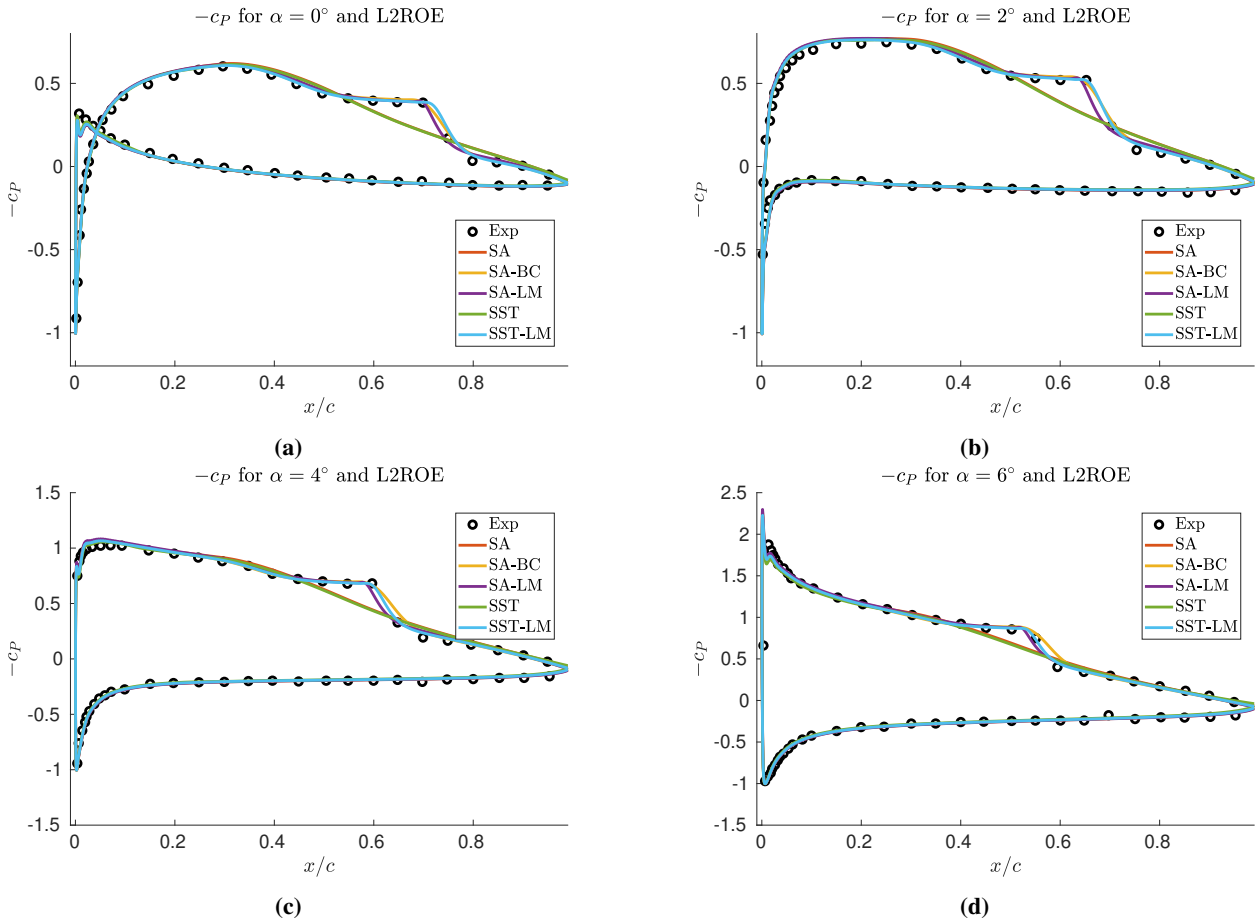

Fig. 4 Pressure coefficient distribution over E387 profile with L2ROE scheme

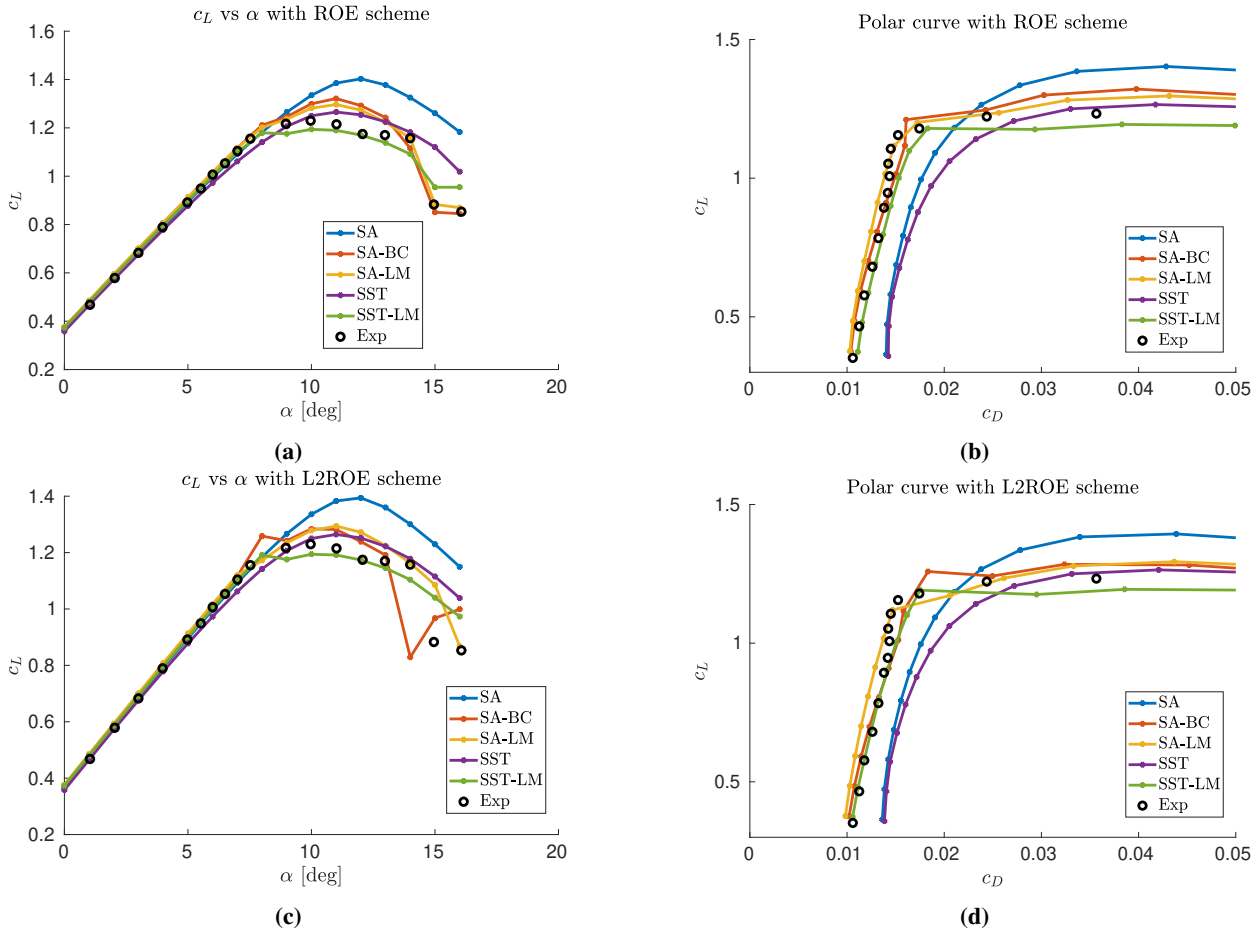

Fig. 5 C_L-α and polar curves for the E387 profile

The polar curves shown in Fig. 5b and Fig. 5d suggest that for lower angles of attack, thus lower values of c_L, the SST-LM and the SA-BC models are consistently better than the SA-LM one, independently on the numerical scheme used. This can be counter-intuitive since the SA-BC model predicts larger laminar separation bubbles. Thus, the region of fully turbulent flow is smaller when compared to the one computed by the SA-LM model. However, the higher value of c_D can be explained by splitting the drag coefficient into its pressure-related ($c_{D,P}$) and friction-related ($c_{D,SFC}$) component, as shown in Fig. 6.

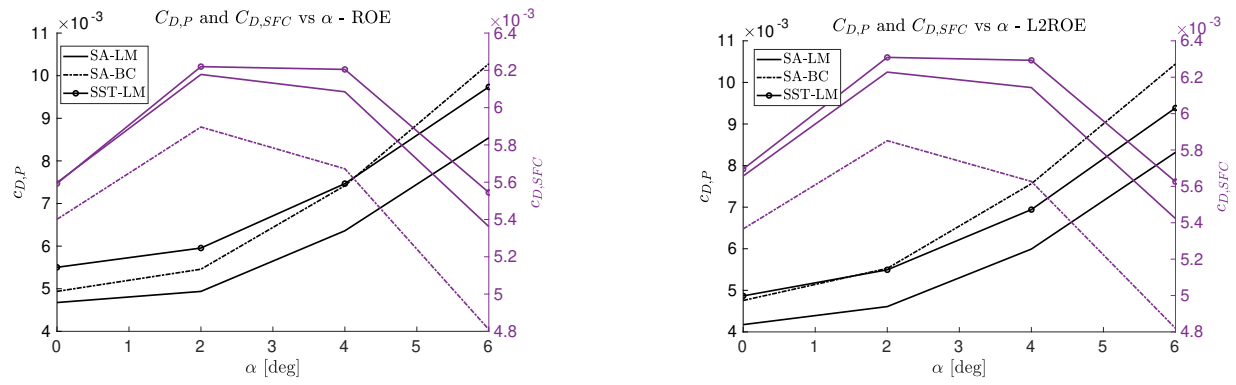

Fig. 6 De-coupling of the drag coefficient components into pressure-related and friction-related for the E387 airfoil: (a) ROE scheme, (a) L2ROE scheme

Taking the results obtained with the ROE scheme, it can be seen that the components computed through the SST-LM model are almost always higher in value than the ones computed through the Spalart-Allmaras model, independently of the transition model chosen. This explains the polar curve of SST-LM being on the right of the SA-LM and SA-BC lines, at least for low values of α. The friction-related drag coefficient from the SA-LM model is always higher than the one computed from the SA-BC model. This has been explained before through the fact that the reattachment point of the laminar separation bubble is consistently downstream for the algebraic model compared to the LM model. However, the BC model's pressure-related drag coefficient is higher, contributing to almost $2/3$ of the total c_D. This is because the larger recirculating zone extends on a region of the airfoil that is directed backward. Thus the pressure acting on the surface is in the direction of the drag. As a result, the predicted drag coefficient is higher for the BC model than for the LM one.

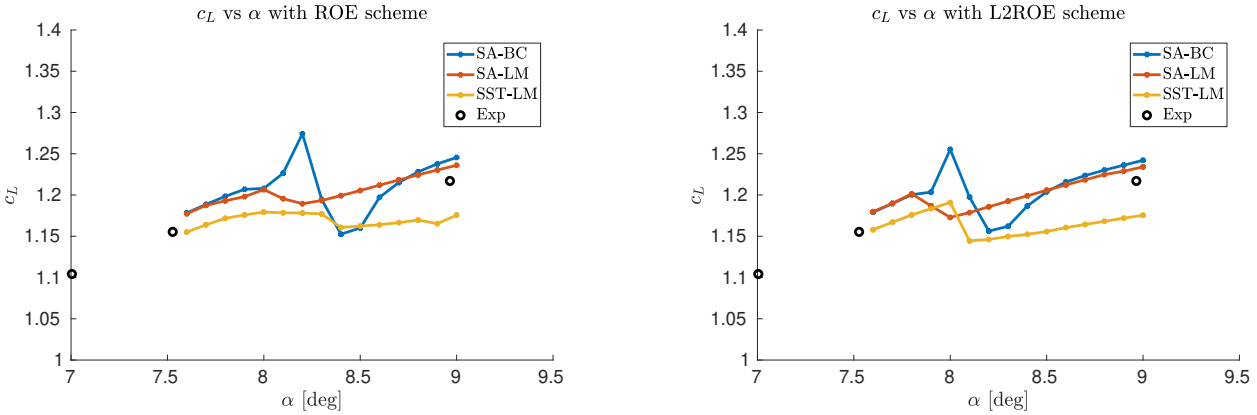

Fig. 7 Zoom of the C_L-α curve for the E387 airfoil and for $\alpha \in [7.6° \div 9°]$: (a) ROE scheme, (b) L2ROE scheme

By inspection of Fig. 5a it can be seen a dip in the C_L values predicted by the SST-LM model between $\alpha = 8° \div 9°$. It can also be seen for the SA-LM and the SA-BC models, even though it seems to have a lower magnitude. By refining the $\Delta\alpha$ used between each simulation to $0.1°$, it has been possible to locate and better investigate the phenomenon. The results of this refinement are reported in Fig. 7. In particular, the BC model seems to have a stronger dip, but then it recovers the c_L very fast, whereas the LM model has a weaker dip followed by a smooth increase of c_L. The angle of attack for which the sudden decrease in c_L appears is different for every model. For the SST-LM, the SA-LM, and the SA-BC model, it starts respectively at $\alpha = 8.3°$, at $\alpha = 8°$, and $\alpha = 8.2°$. To better understand this phenomenon, it is helpful to consider the SST-LM model only and to observe Fig. 8 and Fig. 9. The first picture represents a zoom of the flow field on the leading edge of the profile for three consecutive angles of attack. In particular, the red regions

represent the regions where the X-component of the flow velocity (U) is negative, thus identifying recirculating regions. The second picture represents the X-component of the skin friction coefficient and the pressure coefficient (with a negative sign) over the profile for $\alpha = 8.2° \div 8.5°$. It can be seen that there is the formation of a first, small, laminar separation bubble, which then reattaches shortly after only to separate again, forming a wider re-circulation zone. The region between these bubbles, where the flow is attached, decreases as α increases. This is a consequence of both the first bubble increasing in size and the second bubble slowly reaching the leading edge of the profile. For $\alpha = 8.3°$ the attached region is so small that a further increase in α of 0.1° leads to the two bubbles merging and creating a bigger re-circulation zone. This can be seen both from Fig. 8c, where there is only one red region, and from Fig. 9a, where the yellow markers associated to $\alpha = 8.4°$ remain below the 0 line up until $x/c = 0.1$. Another consequence of this phenomenon is the sudden decrease in the maximum of $-C_P$ on the profile, which is located at the leading edge, the point with higher curvature. This can explain the considerable drop in C_L at $\alpha = 8.4°$ seen in Fig. 7. After this angle of attack, the re-circulation bubble on the LE of the profile decreases in size as α increases, as can be seen from Fig. 9a for $\alpha = 8.5°$. This causes an increase in the region where the flow remains attached after the separation zone, thus leading to an increase in the lift coefficient of the profile.

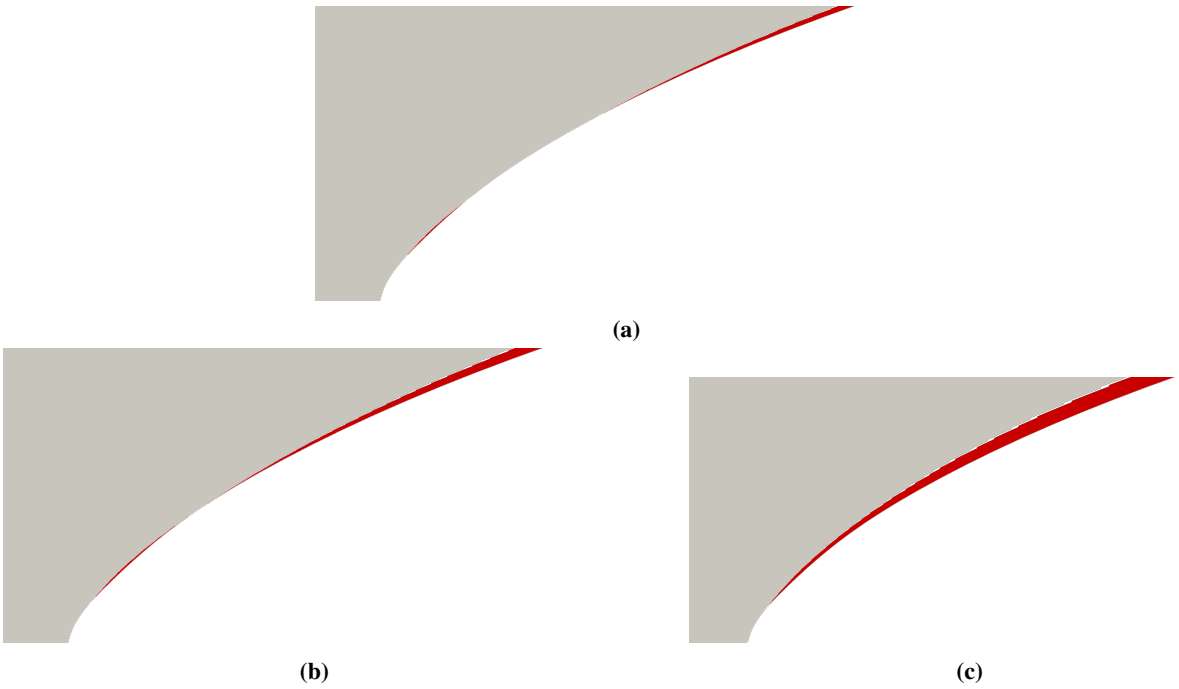

Fig. 8 Zoom on the leading edge of the E387 profile. In red are regions where U < 0: (a) α= 8.2°, (b) α= 8.3°, (c) α= 8.4°

The decreasing trend of the C_L from $\alpha = 8°$ can be explained by the increasing size of the first separation bubble. The SA-LM and the SA-BC model show the same behavior, which tends to point to the fact that it may not be a problem related to the formulation of the transition model. Moreover, even if mesh refinement is considered, this phenomenon does not seem to disappear. In this case, the presence of possible laminar solutions to the turbulence models [24] cannot be discarded as an explanation. In conclusion, this phenomenon requires further investigation since it is not visible from the data extracted from experimental results due to the high $\Delta\alpha$ employed.

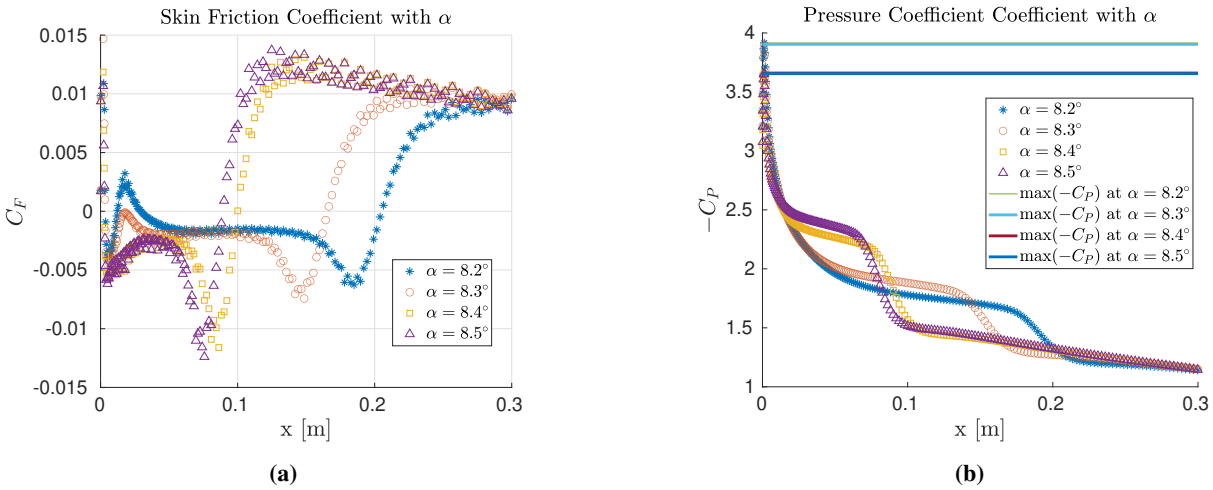

(a) **(b)**

Fig. 9 Focused analysis on the LSBs regions on the E387 profile for four angles of attack: (a) c_F distribution, (b) $-c_P$ distribution

B. 3D Test Cases

The 3D test cases taken into consideration are the Prolate Spheroid [25], studied at DFVLR (now DLR) in Göttingen, Germany, and the Sickle Wing [26], tested at TU Braunschweig. Both cases have been conceived to study the effect of cross-flow (CF) waves on the transition phenomenon. To tackle this problem, the simulations have been performed with the cross-flow extension of the γ-Re_θ model [17] (LM2015). This version allows predicting transition induced by stationary cross-flow instabilities (SFC), which are strongly influenced by the root mean square of the surface roughness (R_a). The results obtained with the original LM model are also reported, highlighting the enhanced version's capabilities.

1. Prolate Spheroid

The 6 : 1 prolate spheroid has been studied due to its geometrically simple shape and its similarities with axisymmetric, aerodynamic bodies, such as fuselages. The geometry is defined through the equation:

$$x^2 + 36y^2 + 36z^2 = \frac{1}{4} \tag{10}$$

where x spans $[-0.5, 0.5]$. The actual shape considered in the experiments and the simulations has a total length of 2.4 m. The test conditions are Mach number $Ma = 0.13$ and Reynolds number $Re = 6.5 \times 10^6$ based on the spheroid length. The reference temperature is 300 K and the freestream turbulence intensity is 0.1%. Three angles of attack have been studied, namely 5°, 10°, and 15°. Depending on the angle of attack, transition on the spheroid's surface is caused by either Tollmien-Schlichting (TS), crossflow (CF) instabilities, or a combination of both. The value of R_a was not provided, thus is assumed to be equal to $3.3\mu\,m$, which is the one of a painted surface. Incompressible simulations have been performed, choosing the FDS scheme to discretize the numerical convective fluxes. MUSCL reconstruction has been used to achieve second-order spatial convergence.

A mesh convergence has been performed on a series of unstructured grids from the 1^{st} AIAA CFD Transition Modeling and Prediction Workshop [27], with increasing prism layers in the boundary layer and surface nodes. The properties of the employed meshes are summarized in Tab. 4, whereas the convergence in terms of c_L and c_D is reported in Fig. 10 for the three angles of attack.

Table 4 Mesh properties for convergence study of 6:1 Prolate Spheroid

Refinement Level	Prism Layers	Surface Nodes	Total Nodes
T (Tiny)	32	1253	53938
C (Coarse)	48	2814	159936
M (Medium)	64	5002	363532
F (Fine)	96	11259	1164171
X (Extra Fine)	128	20026	2715698
U (Ultra Fine)	192	45001	8949137

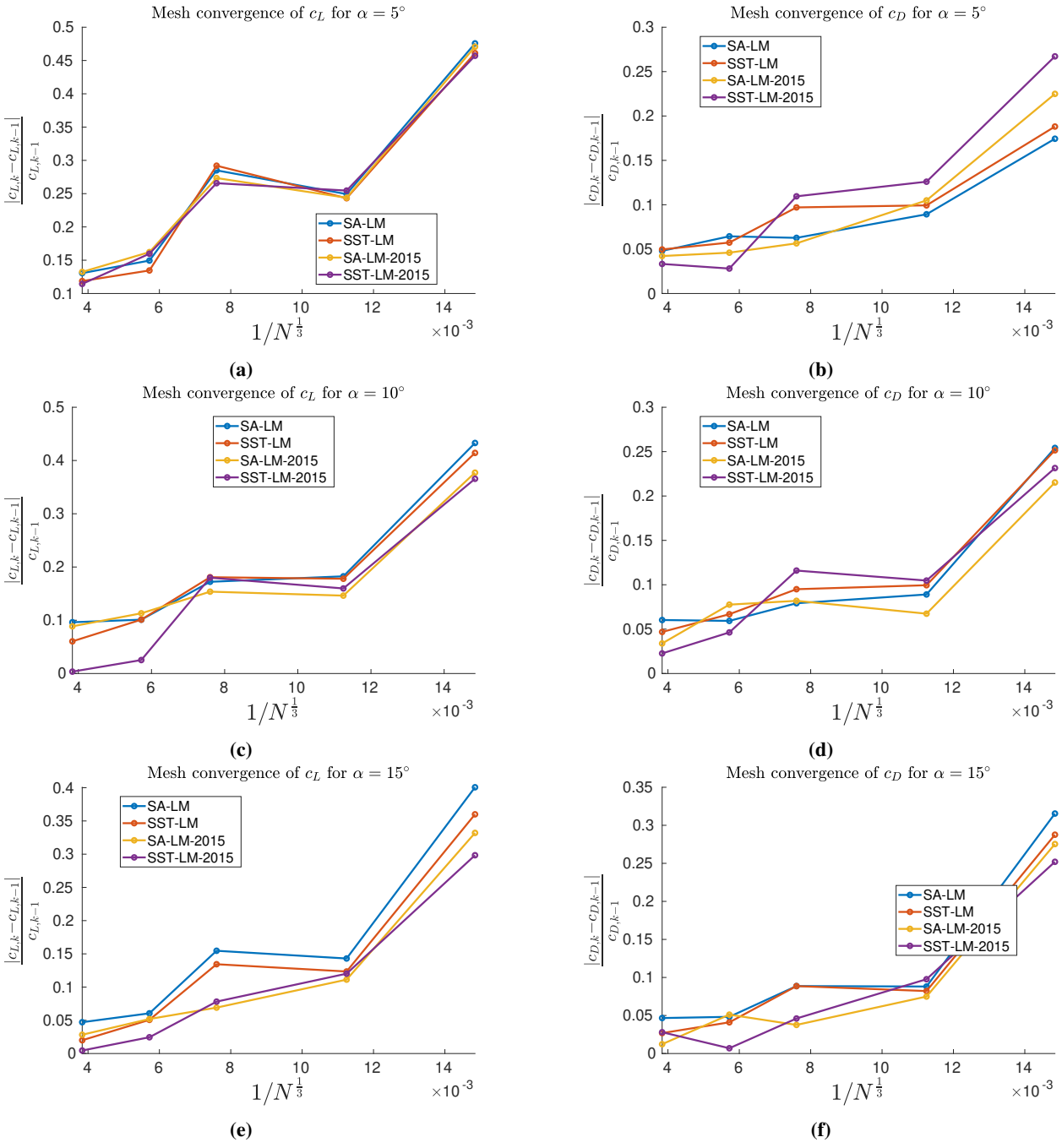

(a) **(b)** **(c)** **(d)** **(e)** **(f)**

Fig. 10 Mesh convergence for the c_L and the c_D of the prolate spheroid

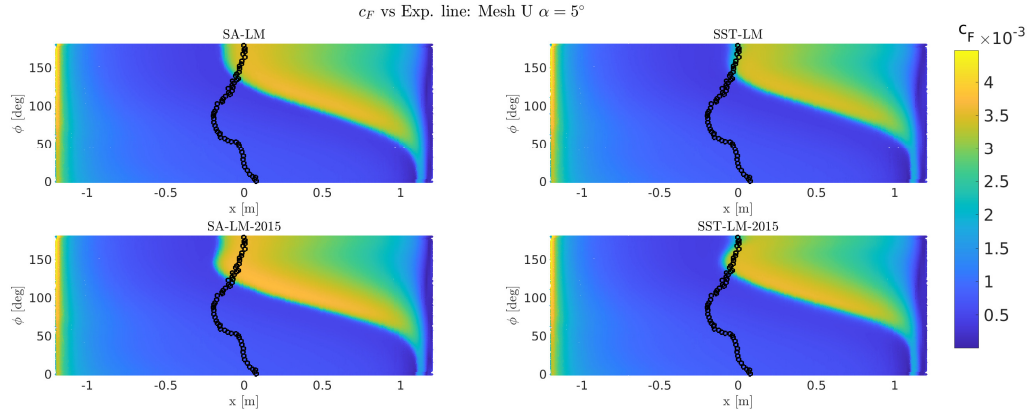

(a)

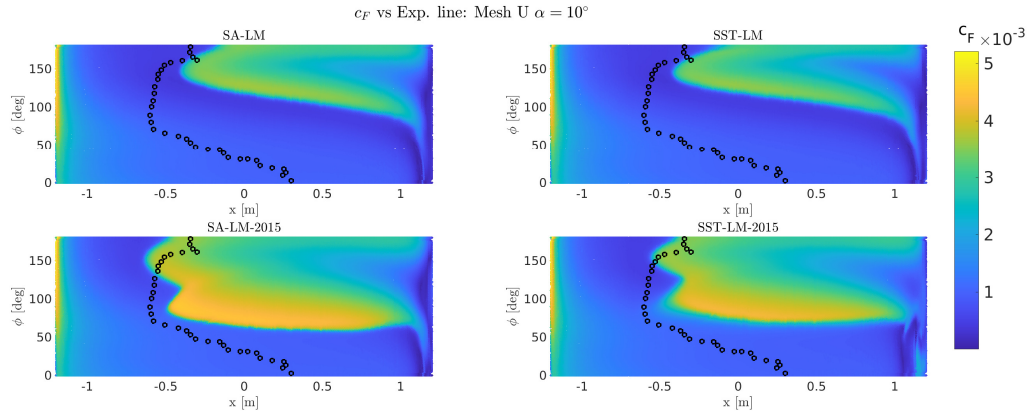

(b)

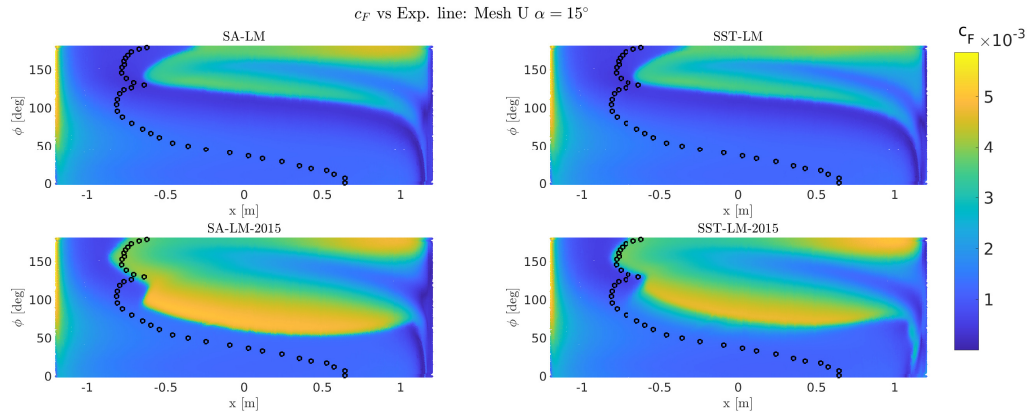

(c)

Fig. 11 Skin friction coefficient distribution on the prolate spheroid for the Ultra-Fine mesh. The black circles refer to the experimental transition line

Mesh convergence has been achieved for all the angles of attack in both the c_L and the c_D. The only problematic case is the convergence for c_L at $\alpha = 5°$, where the variation for the finest mesh is in the order of 10%. A further mesh refinement could be useful to reach less than 10% of convergence for all the angles of attack. Fig. 11 reports the skin friction coefficient distribution over the surface of the prolate spheroid obtained for the finest mesh and the three angles of attack. The black circles represent the experimental transition line. The x-coordinate of the points is represented on the x-axis, whereas the y-axis refers to the azimuthal angle ϕ over the ellipsoid's surface. Such angle is defined such

that, for each yz section of the spheroid, it is equal to 0° for $y_{\phi=0^\circ} = 0$ and $z_{\phi=0^\circ} = min(z)$, and to 180° for $y_{\phi=180^\circ} = 0$ and $z_{\phi=180^\circ} = max(z)$, increasing in value in a counter-clockwise fashion.

The original LM model consistently predicts the transition downstream of the experimental results. This is accentuated the more the angle of attack is increased due to the transition being increasingly dependent on crossflow instabilities. When the LM2015 variant is active, the numerical results are in better agreement with the experimental transition line. However, the wind tunnel experiments show a wider turbulence region in the lower portion of the ellipsoid, which is not correctly captured by the RANS simulations, independently of the angle of attack considered. The discrepancy is higher for $\alpha = 5°$, where the crossflow effects should be negligible. Indeed, the numerical results are quite similar regardless of the usage of the enhanced model. Thus, it seems that is related either to an incorrect assumption on the RMS of the roughness over the surface of the prolate spheroid or to a transition mode that is not taken into account of in the model. It is interesting to notice that the SA-LM couple always predicts transition upstream of the SST-LM model, probably due to the natural decay of the free-stream turbulence intensities associated with the SST model.

2. Sickle Wing

The Sickle wing was studied during the 2015 measurement campaign in the DNW-NWB wind tunnel. It represents an excellent test case for crossflow-induced transition due to the increasing sweep angles along the span. Three sections can be defined: section **A** has a sweep angle of 30°, section **B** has a sweep angle of 45°, and section **C** has a sweep angle of 55°. The model geometry is shown in Fig. 12a. The test section of the wind tunnel has dimensions of 3.25 m × 2.80 m × 8.0 m and is shown in Fig. 12b. Infrared thermography images of the upper and lower surfaces of the model are available to compare the numerical and experimental transition lines. Moreover, the Sickle Wing has been equipped with pressure taps to measure the pressure coefficient distribution for three XZ slices positioned at half of each section along the wing's span. These measurements come without corrections for the wind tunnel walls. Four test conditions have been studied and are summarized in Tab. 5. The free-stream turbulence intensity is equal to 0.05% and the RMS of the roughness on the wing surface is $R_a = 1.47 \times 10^{-6}$. The Reynolds number is referred to a chord of 0.8 m.

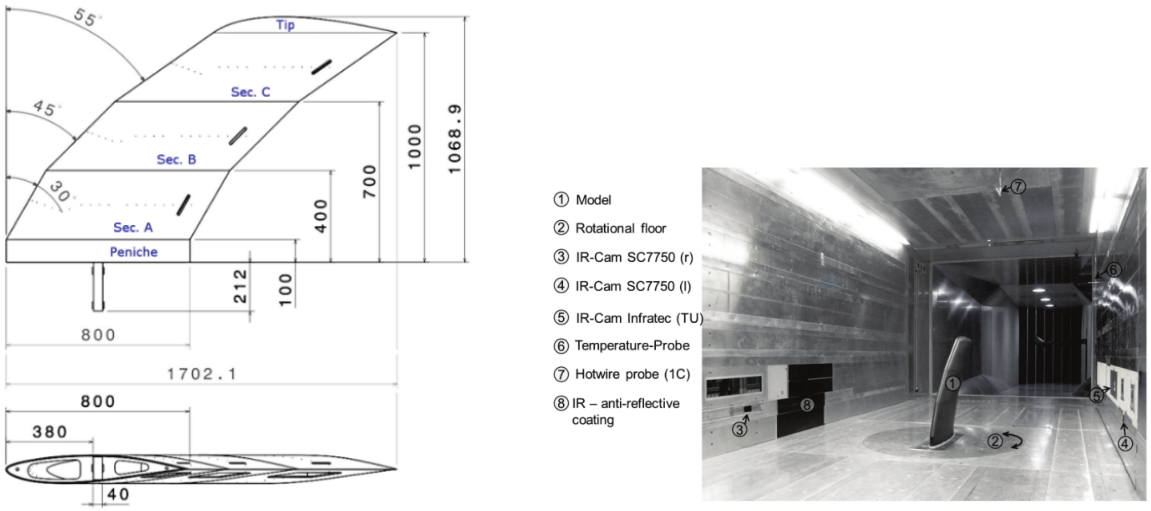

(a) **(b)**

Fig. 12 Sickle wing experiments: (a) Sketch of the Sickle Wing model (all dimensions in mm), (b) wing model mounted in the DNW-NWB wind tunnel

Due to the high computational cost required, a mesh convergence study has not been performed for this test case. The meshes used are unstructured, with a hexahedral boundary layer. The surface mesh is a quad-dominant unstructured grid with 360 spanwise points on the leading edge, 833 spanwise points on the trailing edge, and 300 chordwise points at the junction between different sweep angle sections. Simulations have been performed with and without considering the wind tunnel walls for all the test cases but Case C since the angle of attack is small and the blockage effects are negligible. Free-air simulations have symmetry and far-field boundaries at 50 chord lengths away from the wing. Wind

Table 5 Test conditions for the Sickle Wing

Test name	α [deg]	Re	Ma	U_∞ [m/s]	T_∞[K]	ρ_∞ [kg/m^3]
A	−2.6	2.744×10^6	0.156	53.77	295.77	1.1652
B	−2.6	4.448×10^6	0.259	90.13	301.53	1.14368
C	−0.3	4.434×10^6	0.259	90.16	302.12	1.14144
D	6	2.748×10^6	0.158	54.85	299.12	1.15393

tunnel simulations consider only the straight portion of the testing facility, whose surfaces are modelled as no-slip walls. Incompressible simulations have been performed, employing the FDS scheme for the convective fluxes discretization. MUSCL reconstruction has been used to achieve second-order spatial convergence.

Case A The predicted skin friction distribution for the free-air and wind tunnel simulations is reported respectively in Fig. 13 and Fig. 14. No appreciable difference can be seen regarding the central portion of the wing's upper and lower surface. A rapid upstream movement of the transition location is visible at the first kink between the 30° and 45° sweep angle sections. In section B, an undulating pattern is visible, typical of crossflow transition. The experimental results at the center of section B show another turbulent wedge caused by the pressure taps, which the numerical simulation cannot capture. Between sections B and C, a laminar-separated vortex causes a rise in the transition location, which then proceeds to straighten out. At the end of section C, the laminar region increasingly extends toward the trailing edge, indicating the presence of a different transition mode. The significant difference between the free-air and the wind tunnel simulations is located at the root of the wing. Due to the no-slip boundary condition imposed on the wind tunnel walls, the already developed turbulent boundary layer impacts the wing surface. Compared to the experimental transition line, the height of the side-wall boundary layer seems overpredicted by the numerical simulations. Nevertheless, the presence of a turbulent boundary layer at the root of the wing does not seem to affect the transition prediction on the remaining sections.

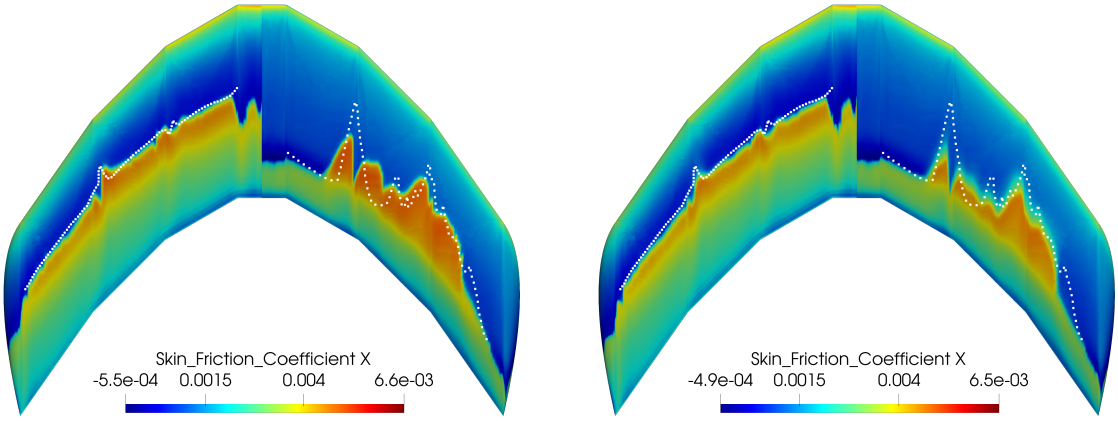

(a) **(b)**

Fig. 13 Skin friction coefficient distribution on the Sickle wing for Case A. The white circles refer to the experimental transition line. (a) SA-LM-2015 model, (b) SST-LM-2015 model. The model is reflected along the XZ and the XY planes for each sub-figure: the left half represents the lower surface, and the right half represents the upper surface.

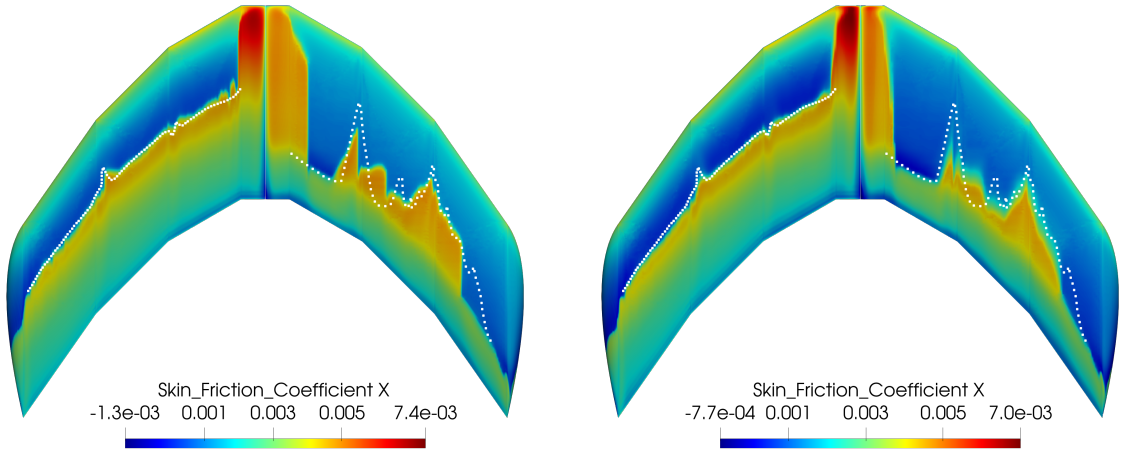

(a) **(b)**

Fig. 14 Skin friction coefficient distribution on the Sickle wing for Case A. Simulation performed with no-slip wind tunnel walls. The white circles refer to the experimental transition line. (a) SA-LM-2015 model, (b) SST-LM-2015 model. The model is reflected along the XZ and the XY planes for each sub-figure: the left half represents the lower surface, and the right half represents the upper surface.

The pressure coefficient distribution for three chordwise slices is reported in Fig. 14. The results obtained by considering the wind tunnel walls are slightly in better agreement with experimental points, indicating that the blockage effect is almost negligible. For the inboard section A, the pressure distribution points to a transition induced by a laminar separation bubble, which is not captured by the numerical simulations. A mesh convergence could point to an under-resolution of the flow in that region or a problem related to the transition modeling.

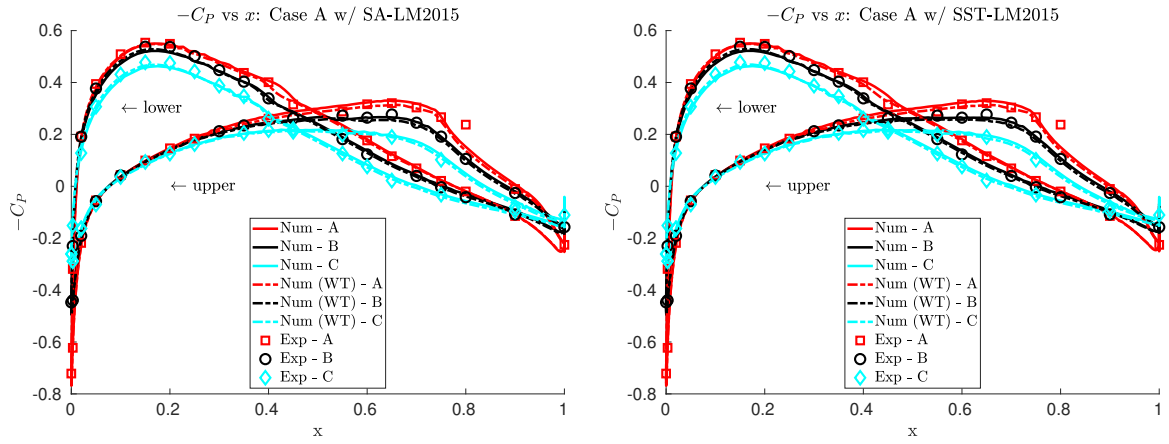

(a) **(b)**

Fig. 15 Distribution of the pressure coefficient over the Sickle wing for Case A

Case B For this case, the Reynolds number has been increased by increasing the air speed from ~ 50 m/s to ~ 90 m/s. Case B aimed to create a more Tollmien–Schlichting (TS) dominated transition on the upper surface with a more gradual increase in the TS amplification rates. The skin friction coefficient distribution is reported in Fig. 16 for the free-air simulation and in Fig. 17 for the wind tunnel one. Overall the transition line moves upstream in both the numerical and experimental results due to the increase in the Reynolds number. However, in the experiments, section A's inboard seems to incur a transition induced by a laminar separation of the boundary layer. Once again, looking at the free-air simulations, CFD fails to predict this phenomenon, thus computing natural transition. As in case A,

transition due to LSBs can be seen on the inner-most portion of the upper surface. Nevertheless, this is only possible due to the absence of the turbulent boundary layer of the wind tunnel's side walls. The remaining portion of the upper surface sees a complete switch to crossflow-induced transition. The turbulent wedges at the kinks between adjacent sections are still visible but not as strong as in case A. On the lower surface, the transition line assumes a *zig-zag* like pattern, pointing to CF-induced transition. Free-air and WT simulations agree with experimental results on most wing surfaces. However, Fig. 17 indicates that the turbulent boundary layer associated with the lateral surface of the test facility and impacting the wing is over-predicted against experimental results. Moreover, the SST-LM205 simulation does not predict cross-flow transition on the upper surface of section B. This seems to be related to a premature end of the simulation since a similar, but smaller pattern is visible in Fig. 16b.

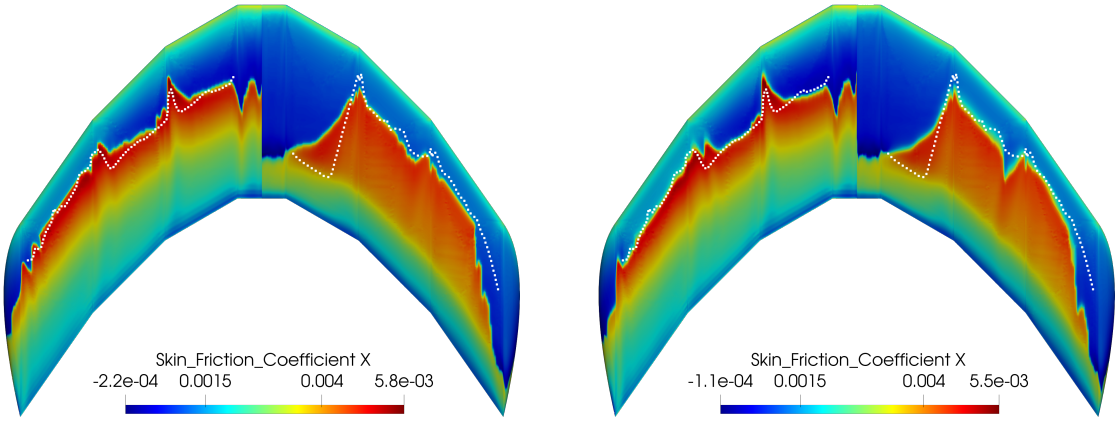

(a) **(b)**

Fig. 16 Skin friction coefficient distribution on the Sickle wing for Case B. The white circles refer to the experimental transition line. (a) SA-LM-2015 model, (b) SST-LM-2015 model. The model is reflected along the XZ and the XY planes for each sub-figure: the left half represents the lower surface, and the right half represents the upper surface.

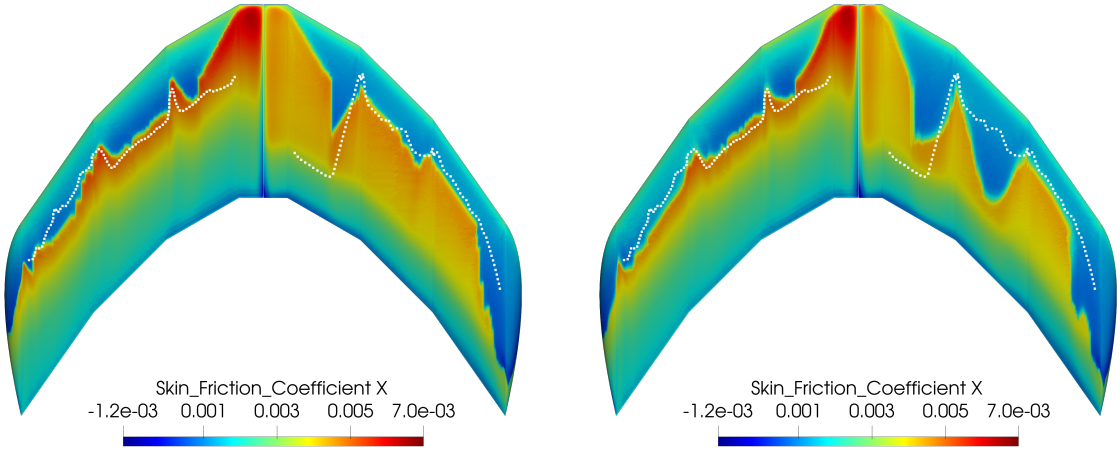

(a) **(b)**

Fig. 17 Skin friction coefficient distribution on the Sickle wing for Case B. Simulation performed with no-slip wind tunnel walls. The white circles refer to the experimental transition line. (a) SA-LM-2015 model, (b) SST-LM-2015 model. The model is reflected along the XZ and the XY planes for each sub-figure: the left half represents the lower surface, and the right half represents the upper surface.

It is interesting to notice how the increase in Reynolds number does not change the pressure distribution when compared against case A, as reported in Fig. 18. As with Case A, numerical results agree reasonably well with experimental data.

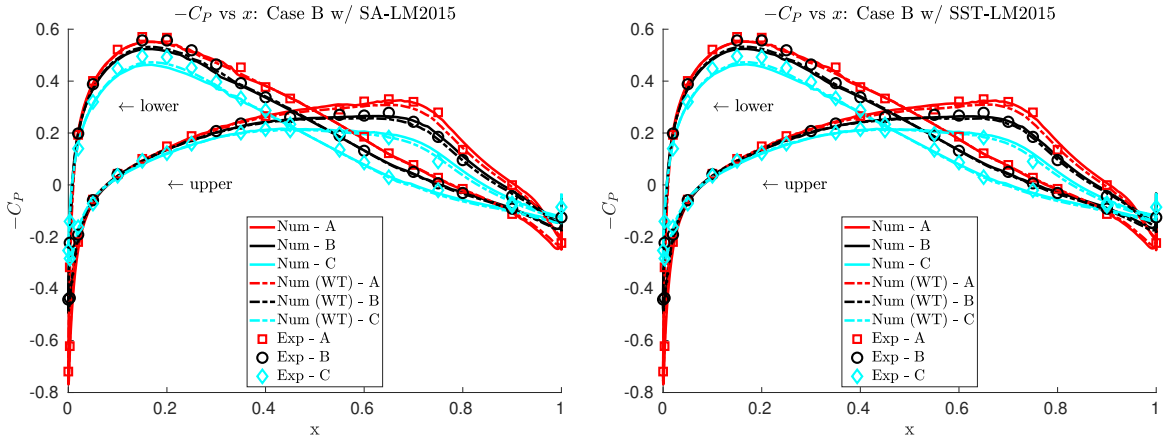

(a) **(b)**

Fig. 18 Distribution of the pressure coefficient over the Sickle wing for Case B

Case C This case has the same Reynolds number as case B, but at $\alpha = -0.3°$ instead of $\alpha = -2.6°$. The lower angle of attack seems to weaken the crossflow-induced transition on the wing's upper surface. There is no difference in section A, where LSBs cause a straight transition line. However, section B presents a mixed-mode transition due to local chordwise changes in the transition location. Section C remains associated with CF instabilities due to the high sweep angle. On the lower surface, the zig-zag pattern of section B points to the CF-dominated transition, whereas section C shows a mixed-mode transition with a smoother transition line. These phenomena are well captured by the SA-LM2015 model, especially those belonging to the upper surface of section C. The SST-LM model predicts a strong turbulent wedge at the kink between sections B and C, followed by a rapid shift to another transition mode along the remaining span of the wing.

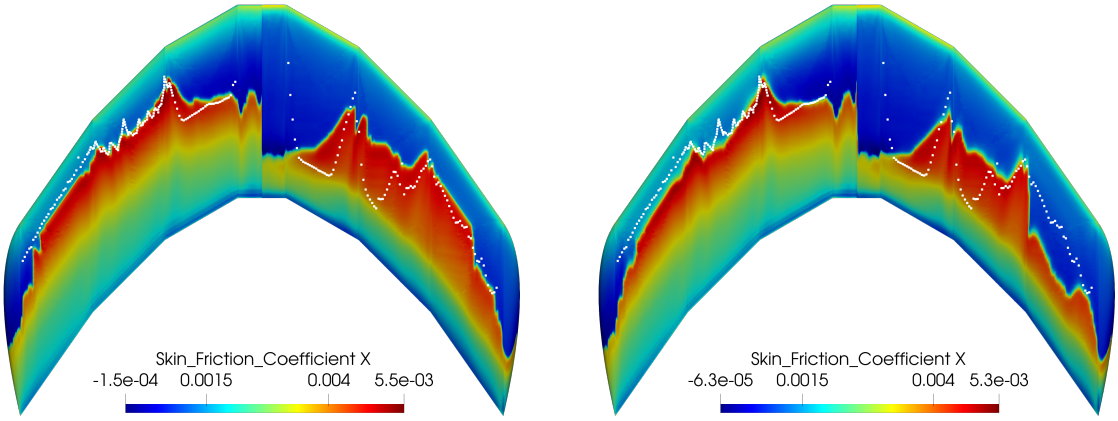

(a) **(b)**

Fig. 19 Skin friction coefficient distribution on the Sickle wing for Case C. The white circles refer to the experimental transition line. (a) SA-LM-2015 model, (b) SST-LM-2015 model. The model is reflected along the XZ and the XY planes for each sub-figure: the left half represents the lower surface, and the right half represents the upper surface.

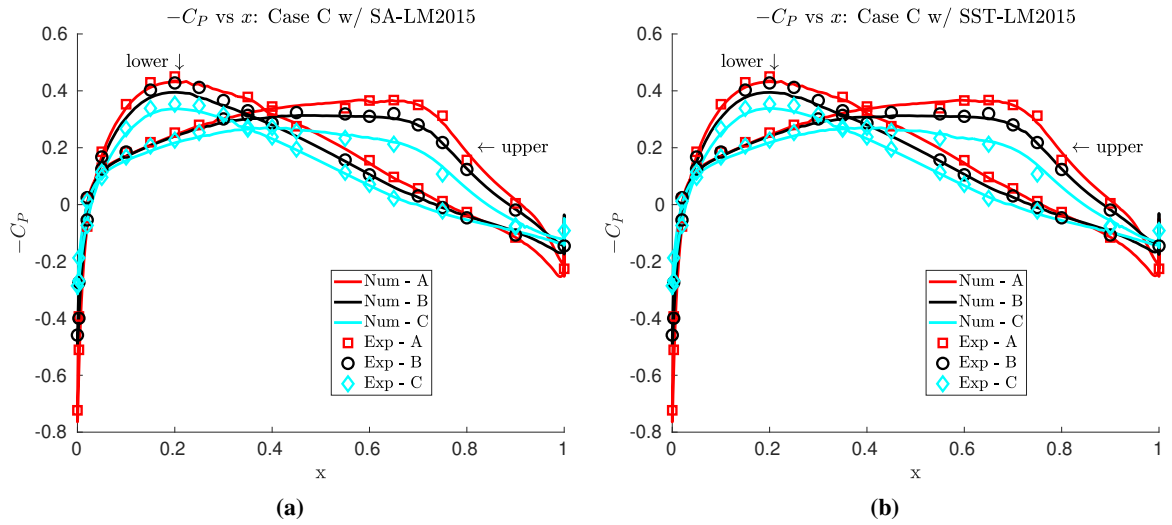

Fig. 20 Distribution of the pressure coefficient over the Sickle wing for Case C

As shown in Fig. 20, the pressure coefficient distributions computed by CFD simulations agree fairly well with the experimental results.

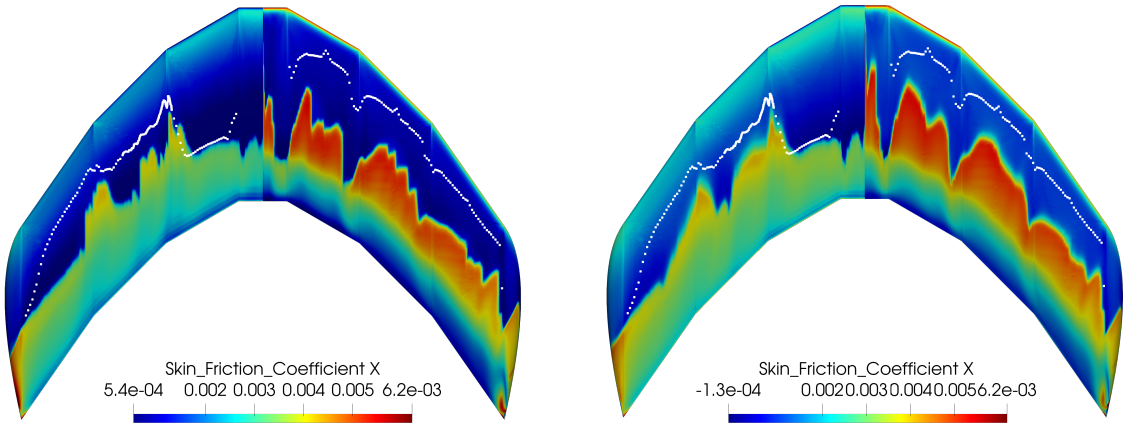

Fig. 21 Skin friction coefficient distribution on the Sickle wing for Case D. The white circles refer to the experimental transition line. (a) SA-LM-2015 model, (b) SST-LM-2015 model. The model is reflected along the XZ and the XY planes for each sub-figure: the left half represents the lower surface, and the right half represents the upper surface.

Case D Case D sees the wing with an angle of attack equal to 6°. As shown in Fig. 21, the increase in α induces a transition pattern utterly different from the previous cases. In particular, on the upper surface, the transition line becomes smooth and moves upstream due to the high adverse pressure gradient. This is associated with Tollmien–Schlichting (TS) instabilities, which dominate the transition over the entire upper surface. Some spikes are visible due to the pressure taps causing early transition. The kinks between the sections now seem to have an opposite effect than the one seen in cases A, B, and C. In particular, they cause a delay in the transition, which is well-captured by the numerical simulations. On the lower surface, the transition on section A is dominated by TS instabilities due to the smooth transition line. Section B shows a switch to CF modes, whereas section C returns to TS instabilities. Here, the kinks show the usual pattern of anticipating the transition location. By comparing Fig. 21 against Fig. 22 it is evident that the simulations performed with the model in the wind tunnel perform marginally better than those in free-air, especially when the upper

surface is considered. Also, the side walls' turbulent boundary layer size seems well captured by the SA-LM2015 model but slightly overpredicted by the SST-LM205 one.

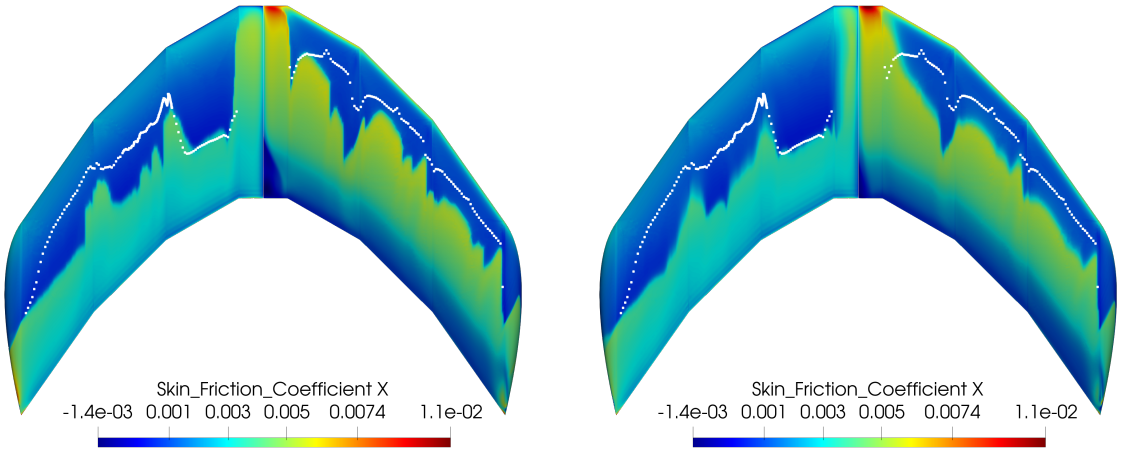

(a) **(b)**

Fig. 22 Skin friction coefficient distribution on the Sickle wing for Case D. Simulation performed with no-slip wind tunnel walls. The white circles refer to the experimental transition line. (a) SA-LM-2015 model, (b) SST-LM-2015 model. The model is reflected along the XZ and the XY planes for each sub-figure: the left half represents the lower surface, and the right half represents the upper surface.

The pressure coefficient distribution reported in Fig. 23 highlights the importance of considering the wind tunnel walls in the computation. The high angle of attack increases the wing's blockage effect, explaining the visible differences between the free-air and the wind tunnel simulations.

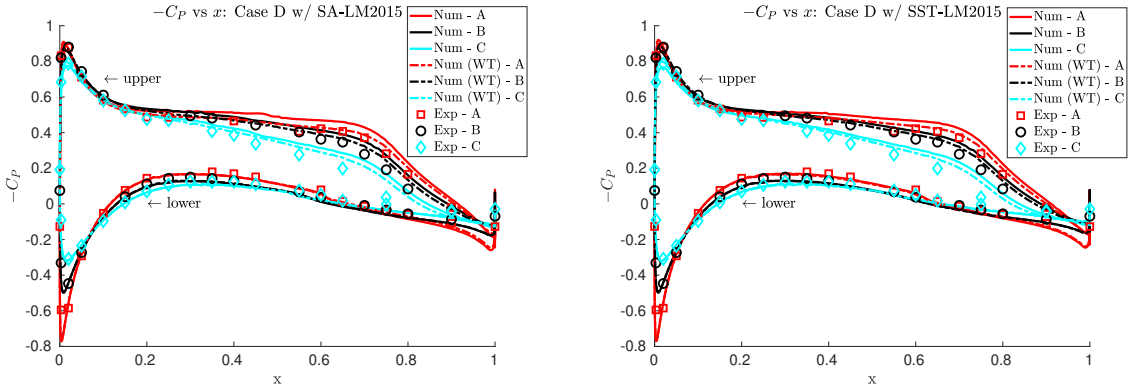

(a) **(b)**

Fig. 23 Distribution of the pressure coefficient over the Sickle wing for Case D

IV. Conclusions

In the present work, the Langtry-Menter transition model has been implemented within the open source framework SU2 by coupling it with the Menter SST and the Spalart-Allmaras turbulence model. The correctness of the implementation has been verified against 2D and 3D experimental results. The ERCOFTAC and the Schubauer and Klebanoff Zero-Pressure-Gradient flat plate test cases have been used as model benchmarks due to their wide use in literature. A good agreement has been reached over all the test cases on the transition onset location. However, the transition region is under-predicted in two test cases compared to experimental results.

In order to assess the capability of the model to predict aerodynamic performances for aerospace-related applications, the flow around the Eppler E387 profile has been investigated. The lift coefficient is well recovered on the whole range of angles of attack, including the post-stall region. The drag coefficient is also in good agreement over the pre-stall region, whereas it is over-predicted for higher angles of attack. This behavior, however, is also present with another transition model and for fully-turbulent simulations, thus indicating that it is not a limitation of the implemented model. A decrease in lift coefficient around $\alpha = 8^\circ$ has been found and discussed. This can be re-conducted to the formation and the increase in the size of a small laminar separation bubble, which merges with a wider and adjacent re-circulation zone, thus leading to a sudden drop in pressure coefficient at the leading edge. This phenomenon, however, does not have an experimental verification due to the high values of $\Delta\alpha$ used for the experimental campaign. Thus, it needs further investigation.

Two 3D test cases have been studied, namely the inclined prolate spheroid and the Sickle wing. To study the transition induced by stationary crossflow waves, the LM2015 extension to the original model has been implemented, which adds new correlations to tackle this problem.

The prolate spheroid has been simulated for three different angles of attack to increase the influence of the crossflow-induced transition. A mesh convergence study has been performed employing six meshes with an increasing number of cells. Numerical results agree with experimental data on the upper portion of the geometry. However, contrary to the real-world data, CFD predicts laminar flow on the lower region even for the higher angle of attack. This can be associated with the arbitrary assignment of a value to the root mean square of the roughness of the ellipsoid surface.

The Sickle wing problem is an excellent test due to its spanwise sections at different sweep angles and test conditions. A mix of transition modes from Tollmien–Schlichting instabilities to crossflow waves occurs on the surface, thus challenging the numerical transition model. Free-air and wind tunnel simulations have been performed to check the importance of the blockage effect. Overall, good agreement has been reached between numerical and experimental results in transition line prediction and pressure coefficient distribution computation. Wind tunnel simulations consistently performed better than free-air ones, even if only marginally for most of the test cases.

Acknowledgments

This project has received funding from the Clean Sky 2 Joint Undertaking (JU) under grant agreement No 101008257. The JU receives support from the European Union's Horizon 2020 research and innovation programme and the Clean Sky 2 JU members other than the Union.

References

[1] Smith, A. M. O., "Transition, pressure gradient and stability theory," *Douglas Aircraft Co., Report ES 26388*, 1956.

[2] Van Ingen, J., "A suggested semi-empirical method for the calculation of the boundary layer transition region," *Technische Hogeschool Delft, Vliegtuigbouwkunde, Rapport VTH-74*, 1956.

[3] Jones, W. P., and Launder, B., "The calculation of low-Reynolds-number phenomena with a two-equation model of turbulence," *International Journal of Heat and Mass Transfer*, Vol. 16, No. 6, 1973, pp. 1119–1130.

[4] Rodi, W., and Scheuerer, G., "Calculation of laminar-turbulent boundary layer transition on turbine blades," *NASA STI/Recon Technical Report N*, Vol. 86, 1985, p. 29839.

[5] Abu-Ghannam, B., and Shaw, R., "Natural transition of boundary layers—the effects of turbulence, pressure gradient, and flow history," *Journal of Mechanical Engineering Science*, Vol. 22, No. 5, 1980, pp. 213–228.

[6] Menter, F., Esch, T., and Kubacki, S., "Transition modelling based on local variables," *Engineering Turbulence Modelling and Experiments 5*, Elsevier, 2002, pp. 555–564.

[7] Menter, F. R., Langtry, R. B., Likki, S., Suzen, Y., Huang, P., and Völker, S., "A correlation-based transition model using local variables—part I: model formulation," 2006.

[8] Langtry, R. B., Menter, F., Likki, S., Suzen, Y., Huang, P., and Völker, S., "A correlation-based transition model using local variables—part II: test cases and industrial applications," 2006.

[9] Mura, R., and Cakmakcioglu, S. C., "A revised one-equation transitional model for external aerodynamics-part i: Theory, validation and base cases," *AIAA Aviation 2020 Forum*, 2020, p. 2714.

[10] Kubacki, S., and Dick, E., "An algebraic model for bypass transition in turbomachinery boundary layer flows," *International Journal of Heat and Fluid Flow*, Vol. 58, 2016, pp. 68–83.

[11] Palacios, F., Alonso, J., Duraisamy, K., Colonno, M., Hicken, J., Aranake, A., Campos, A., Copeland, S., Economon, T., Lonkar, A., et al., "Stanford university unstructured (SU2): an open-source integrated computational environment for multi-physics simulation and design," *51st AIAA aerospace sciences meeting including the new horizons forum and aerospace exposition*, 2013, p. 287.

[12] Menter, F. R., "Two-equation eddy-viscosity turbulence models for engineering applications," *AIAA journal*, Vol. 32, No. 8, 1994, pp. 1598–1605.

[13] Spalart, P., and Allmaras, S., "A one-equation turbulence model for aerodynamic flows," *30th aerospace sciences meeting and exhibit*, 1992, p. 439.

[14] Langtry, R. B., and Menter, F. R., "Correlation-based transition modeling for unstructured parallelized computational fluid dynamics codes," *AIAA journal*, Vol. 47, No. 12, 2009, pp. 2894–2906.

[15] Grabe, C., and Krumbein, A., "Extension of the γ-Reθt model for prediction of crossflow transition," *52nd Aerospace Sciences Meeting*, 2014, p. 1269.

[16] Kaynak, Ü., "Supersonic boundary-layer transition prediction under the effect of compressibility using a correlation-based model," *Proceedings of the Institution of Mechanical Engineers, Part G: Journal of Aerospace Engineering*, Vol. 226, No. 7, 2012, pp. 722–739.

[17] Langtry, R., "Extending the gamma-rethetat correlation based transition model for crossflow effects," *45th AIAA fluid dynamics conference*, 2015, p. 2474.

[18] D'Alessandro, V., Montelpare, S., Ricci, R., and Zoppi, A., "Numerical modeling of the flow over wind turbine airfoils by means of Spalart–Allmaras local correlation based transition model," *Energy*, Vol. 130, 2017, pp. 402–419.

[19] Savill, A., "Some recent progress in the turbulence modelling of by-pass transition," *Near-wall turbulent flows*, 1993, pp. 829–848.

[20] Savill, A., "One-point closures applied to transition," *Turbulence and transition modelling*, Springer, 1996, pp. 233–268.

[21] Schubauer, G. B., and Klebanoff, P. S., "Contributions on the mechanics of boundary-layer transition," Tech. rep., 1955.

[22] McGhee, R. J., *Experimental results for the Eppler 387 airfoil at low Reynolds numbers in the Langley low-turbulence pressure tunnel*, Vol. 4062, National Aeronautics and Space Administration, Scientific and Technical . . . , 1988.

[23] Malan, P., Suluksna, K., and Juntasaro, E., "Calibrating the-re transition model for commercial cfd," *AIAA Paper*, Vol. 1142, 2009.

[24] Rumsey, C. L., "Apparent transition behavior of widely-used turbulence models," *International Journal of Heat and Fluid Flow*, Vol. 28, No. 6, 2007, pp. 1460–1471.

[25] Kreplin, H., Vollmers, H., and Meier, H., "Wall shear stress measurements on an inclined prolate spheroid in the DFVLR 3 m× 3 m low speed wind tunnel," *Data Report, DFVLR IB*, 1985, pp. 222–84.

[26] Kruse, M., Munoz, F., Radespiel, R., and Grabe, C., "Transition prediction results for sickle wing and NLF (1)-0416 test cases," *2018 AIAA Aerospace Sciences Meeting*, 2018, p. 0537.

[27] "1st AIAA CFD Transition Modeling and Prediction Workshop," `https://transitionmodeling.larc.nasa.gov/workshop_i/`, 2021.